Spectrochimica Acta Part B 158 (2019) 105644

Contents lists available at ScienceDirect

Spectrochimica Acta Part B

journal homepage: www.elsevier.com/locate/sab

Species distribution in laser-induced plasma on the surface of binary immiscible alloy

Yang Zhao[a], Lei Zhang[a,b,*], Jiajia Hou[a], Weiguang Ma[a,b], Lei Dong[a,b], Wangbao Yin[a,b], Liantuan Xiao[a,b], Suotang Jia[a,b], Jin Yu[c]

[a] State Key Laboratory of Quantum Optics and Quantum Optics Devices, Institute of Laser Spectroscopy, Shanxi University, Taiyuan 030006, China
[b] Collaborative Innovation Center of Extreme Optics, Shanxi University, Taiyuan 030006, China
[c] School of Physics and Astronomy, Shanghai Jiao Tong University, Shanghai 200240, China

ARTICLE INFO

Keywords:
Species distribution
Laser-induced breakdown spectroscopy (LIBS)
Laser-induced plasma (LIP)
Laser-supported absorption (LSA) wave

ABSTRACT

Investigation on species distribution of vapor plasma is of great significance for understanding the laser-target interaction, the plasma dynamics and verifying theoretical models. It is also helpful for optimizing the spectral acquisition to improve the quantitative performance of spatial-resolved laser-induced breakdown spectroscopy (LIBS). In this work, the laser-induced plasma on the surface of binary alloy is analyzed by using spectrally, spatially and temporally resolved dual-wavelength differential imaging to explore the dependence of species distribution in plasma on laser-supported absorption (LSA) wave regime and sample composition. The laser-supported combustion (LSC) and laser-supported detonation (LSD) wave dominated plasmas with different elemental mass ratios are induced from a series of binary immiscible alloys by using low and high irradiance laser pulses, respectively. By comparing the spatial-temporal emissivity images of species, the following conclusions are drawn: 1) laser irradiance can change the species distribution of plasma, while the sample composition cannot; 2) for LSC-wave dominated plasma, the species distribution mainly depends on the melting points of constituted elements in the sample, while for LSD-wave dominated plasma, it mainly depends on the atomic masses of elements. The above behaviours on species distribution in plasma produced from binary immiscible alloys are expected to be suitable for other elements or even multi-element plasmas.

1. Introduction

Laser-induced plasma (LIP) as a spectroscopic emission source has been studied in earnest since the 1960s. The LIP emits characteristic lines during its expansion cooling. Qualitative or quantitative analysis of unknown sample can be achieved by analyzing these spectral lines. This technique is called laser-induced breakdown spectroscopy (LIBS), which is known as “next superstar” within the group of analytical atomic spectrometry methods [1]. It is expected to be widely used in industrial process monitoring, such as chemical industry [2–4], metallurgy [5], etc., for its capability of fast speed and multi-element analysis. Because the LIP contains complex radiation and species, the internal structure of it is rather ambiguous. The significance of investigation on species distribution of LIP mainly manifests in three aspects: understanding more deeply the complex phenomena involved in laser-target interaction and the dynamics of LIP, providing a means of experimental verification for theoretical models, and improving the quantitative performance of spatially-resolved LIBS through optimization of optical collection parameters.

Previous work on plasma species distribution mainly focused on either initial evolution model or experimental observations. For plasma evolution, the laser-supported absorption (LSA) wave model was firstly proposed by Raizer [6] in 1966 and progressively improved [7–12]. Attributing to different experimental conditions such as laser irradiance, wavelength, target vapor composition, ambient gas composition, gas pressure, etc., the LSA-wave usually has two regimes of wave propagation, the laser-supported combustion (LSC) wave and the laser-supported detonation (LSD) wave. The difference between them mainly arises from different mechanisms used to propagate the absorbing front into the cool transparent atmosphere. For experimental studies, the distribution images of species were taken by means of two-dimensional spectral scanning or CCD imaging. For example, Cristoforetti et al. studied the distribution of Al species from the target and air species in plasma and provided important information about the formation of

* Corresponding author at: State Key Laboratory of Quantum Optics and Quantum Optics Devices, Institute of Laser Spectroscopy, Shanxi University, Taiyuan 030006, China.
E-mail address: k1226@sxu.edu.cn (L. Zhang).

https://doi.org/10.1016/j.sab.2019.105644
Received 26 March 2019; Received in revised form 28 June 2019; Accepted 28 June 2019
Available online 03 July 2019
0584-8547/

plasma and its successive evolution history [13]. Aguilera and Aragón et al. studied the relative distributions of Fe and Ar atoms in plasma and deemed that there was an important interaction between plasma and the surrounding atmosphere [14–17]. They also obtained the three-dimensional distributions of the neutral atoms and ions of Ni, Fe, and Al in the plasma [18,19]. Bulatov et al. confirmed that Cu and Zn species mainly present at a different location in the plasma by drawing the species intensity distribution map, which is helpful to find the optimum site in the plasma that provides the best spectral signal to noise ratio [20]. Wazzan et al. compared the emission intensities and number densities of Ba II in vacuum and in ambient gas and found that the presence of ambient gas led to a significant increase in local number density at the expanding front of the plasma plume [21]. Geometric factors were investigated by Multari et al. through imaging for Al I, Al II and Ti II species to optimize the excitation and fluorescence collection parameters [22]. Although the above theoretical evolution and experimental research have been thoroughly studied, they were seldom related. Yu et al. experimentally investigated the structure and dynamics of unitary Al plasma in the early stage by using dual-wavelength differential spectroscopic imaging, and explored the mechanism of laser post-ablation interaction [23,24]. It was demonstrated that plasma shielding due to various species localized in different zones inside of the plume led to different morphologies and internal structures of the plasma. Also the differences between LSC- and LSD-wave such as plume morphology, species localized in plasma core, species lifetime, internal plasma structure, decay velocity of population, etc. were investigated [25–27]. The authors pointed out that the characteristics of LSC-wave include a rather spherical expansion of the plume, a layered internal structure, and a fast decay of the ionized population of the ambient gas. The plasma shielding in this case is dominantly contributed by the ablation vapor, which leads to an absorption zone in the middle of the plume close to the target surface. The characteristics of LSD-wave include a clearly elongated morphology of the plume, a dominant plasma core consisting of a mixture of ions of aluminum and argon, and a significantly longer lifetime of argon ions. The plasma shielding in this case is dominantly contributed by the shocked and the ionized ambient gas which is initially localized around the propagation front of the plume. These works mainly investigated on plasmas produced from unitary alloy, no more complex plasmas produced from binary or multi-element alloy were involved.

This paper attempts to further study the spatial-temporal distribution of species in vapor plasmas produced from binary alloys. Here, the species distribution refers specifically to the distribution order of species layers coming from the target. Firstly, LSC- and LSD-wave dominated plasmas will be induced on the surfaces of binary samples by using low and high irradiance laser pulses, respectively. Then, we will investigate the dependence of species distribution on LSA-wave regime and sample composition through dual-wavelength differential spectroscopic imaging. Finally, the resulted conclusions on species distribution in plasma produced from binary immiscible alloy will be validated theoretically and experimentally.

2. Experimental

2.1. Sample

In order to more clearly understand the spatial and temporal distribution of species in plasma produced from binary alloy, Al and Sn were selected due to their significant differences in physical properties (see Table 1) such as melting point, atomic mass and sparse, non-interference characteristic lines. In this experiment, three Al—Sn alloys were used as test samples, of which the mass ratios of Al to Sn were 7:3, 5:5, and 3:7, corresponding to the atomic number density ratios of about 10:1, 4:1, and 2:1, respectively. Note that the Al—Sn alloys are immiscible alloys with a melting point of about 870 K and liquid phase separation characteristics.

2.2. Experimental setup

Fig. 1 displays the schematic of the experimental LIBS setup with differential spectroscopic imaging. A Q-Switched Nd: YAG laser (Spectra Physics, INDIHG-20S) emitted pulses with 7 ns pulse duration and 20 Hz repetition rate at the wavelength of 1064 nm. The laser pulse was reflected by a silver-coated mirror and passed through a half-wave plate (HWP) and was divided into two beams by a polarizing beam splitter (PBS). An absolutely calibrated energy meter (Newport, 2936-R) was used to measure the fraction of the laser reflected by the PBS so as to monitor the incident laser energy. The transmitted laser beam was focused by a plano-convex lens (L1) of 50 mm focal length to produce a focal spot about 0.3 mm in diameter. The sample was loaded on an integrated, motorized, software-controlled X-Y-Z stage to make each laser pulse hit on a fresh spot of the alloy surface. On one side of plasma perpendicular to the axis of laser incidence, an ICCD1 (Andor, iStar DH334T) was used to record the images of plasma species through a 4f system consisting of two lens (L2 and L3) and a narrow band filter (F). On the other side of plasma perpendicular to the axis of laser incidence, a lens (L4) was used to amplify the plasma image by 6 times. The emissions came from different axial (x) and radial (r) positions of the plasma plume were guided to a grating spectrograph (Princeton Instruments, SP-2750) that equipped with a time gated ICCD2 detector (Princeton Instruments, PI-MAX4-1024i) through a 0.2 mm diameter all-silica optical fiber. The fiber was mounted on a software-controlled X-Y stage perpendicular to the sample surface. The wavelength scale of the spectrograph was calibrated by a low pressure Hg-lamp (Newport, 6048) and the spectral intensity was calibrated by a powerful deuterium halogen source (Avantes, AvaLightDH).

More specifically, in the experiment, laser pulses with irradiances of 1 GW/cm^2 and 10 GW/cm^2 were used. Two pipes blew argon at a speed of 5 L/min continuously to make the plasma always be surrounded by pure argon during the experiment. For temporal imaging, delay times of 20, 200, and 400 ns were used, with corresponding gate widths of 2, 5, and 20 ns, respectively.

2.3. Emissivity images of species

For differential spectroscopic imaging, the adequate pair of filters (F1 and F2) was selected for imaging each species of interest. Here, the transmission curve of F1 was centered on a characteristic line of a species to be studied, while that of F2 was shifted to a neighboring wavelength where emission from the species was negligible. Thus the two-dimension emission of the studied species inside the plasma was obtained through the subtraction of the species image from F1 (for species signal) and that from F2 (for continuum background). It should be noted that each image transmitted through the filter was corrected with the corresponding transmission curve so that the images from F1 and F2 were comparable. In order to reduce the fluctuations and improve the signal-to-noise ratio, specific ICCD gain was used for each species imaging (listed in Table 1), and each image was accumulated 60 times. The spectra collected by the fiber aligned with the central part of the amplified plasma image of Al—Sn alloy at 20 ns and 400 ns with laser irradiance of 10 GW/cm^2 is shown in Fig. 2, where the characteristic lines emitted by the six species were identified. The selected lines for representing these species were indicated by letters “a” for Al II, “d” for Al I, “g” for Sn II, “c” for Sn I, “e” for Ar II and “h” for Ar I, while the continuum emissions were indicated by letters “b”, “f” and “i”. The spectroscopic parameters of characteristic lines and central wavelengths of filters for each species were also listed in Table 1. It needs to be mentioned that the Al II line at 358.66 nm is a superposition of 15 lines. Since the bandwidths of the filters are less than 10 nm, the lines emitted by Al, Sn and Ar species did not interfere with each other for spectral imaging. The Abel inversion [28] based on Fourier-Hankel algorithm was used to transform the integral intensity images of species recorded by ICCD into the emissivity ones. To improve the contrast, all

Table 1
Specifications of the physical properties of Al and Sn, the pair of filters selected for the observation of atomic and ionic species of Al, Sn, and Ar and the spectroscopic parameters of these spectral lines. The ICCD gains corresponding to each species under different laser irradiances are also listed.

Element	Melting point (K)	Boiling point (K)	Relative atomic mass	Species	Emission line (nm)	Lower level energy (eV)	Upper level energy (eV)	Transition probability ($\times 10^7$ s^{-1})	Central wavelength of F1 (nm)	Central wavelength of F2 (nm)	ICCD gain	
											1 GW/cm^2	10 GW/cm^2
Aluminum	933	2260	27	Al I	394.40	0.00	3.14	4.99	396	370	200	50
					396.15	0.01	3.14	9.85			200	50
				Al II	358.66	11.85	15.30	23.5	358	370	200	50
Tin	504	2533	119	Sn I	380.10	1.07	4.33	2.80	380	370	200	50
				Sn II	533.23	8.86	11.19	9.90	530	522	500	200
Argon	–	–	–	Ar I	763.51	11.55	13.17	2.45	764	786	500	200
				Ar II	484.78	16.75	19.31	8.49	488	522	500	200
					487.99	17.14	19.68	8.23			500	200

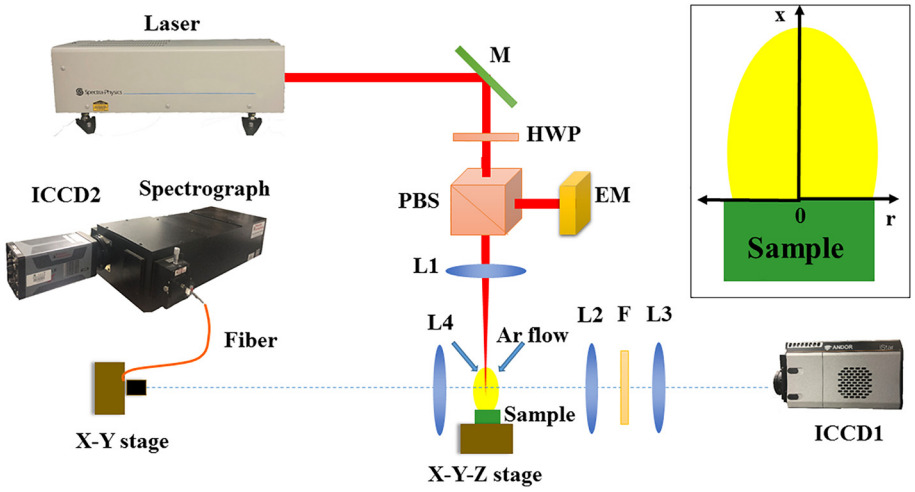

Fig. 1. Schematic of the experimental LIBS setup with differential spectroscopic imaging. M: mirror, HWP: half-wave plate, PBS: polarizing beam splitter, EM: energy meter, L1, L2, L3, L4: lens, F: filter.

the emissivity images were normalized by their maximums and the species were expressed in different colors. Note that it is imprecise to identify the spatial number density distribution of elements by measuring the corresponding distribution of light emitted at specific wavelengths. Because light intensity should also take into account corrections of electron temperature, electron density and pressure gradient of plasma. However, in this work, the light intensity was employed to qualitatively characterize the plasma morphology and the layer structure, but not to quantify the species density. Therefore, there is no need for any correction of spectral line intensity.

3. Results and discussion

In order to study the species distribution in plasmas produced from binary alloy, spatial-temporal emissivity images of Ar I (blue), Ar II (grey), Al I (red), Al II (green), Sn I (goldenrod) and Sn II (fuchsia) species in plasmas induced from the three alloys with different laser irradiances were obtained. The behavior of the species was further compared by plotting the normalized axial emissivity profiles at the middle of the plasma. The effects of LSA-wave regime and sample composition on species distribution in plasmas produced from binary immiscible alloy are discussed as follows.

3.1. Species distribution on LSA-wave regime

3.1.1. Identification of LSA-wave regime

The LSA-wave model on plasma propagation mainly consists of LSC- and LSD-wave regimes. The key to identify the exact regime of an initial plasma is the incident laser irradiance. In our experiment, laser irradiances of 1 GW/cm^2 (close to the breakdown threshold of 0.6 GW/cm^2) and 10 GW/cm^2 were employed to produce plasmas, of which both the emissivity images and normalized central axial emissivity profiles of species at 20 ns are shown in Fig. 3. Compared with the later stage of plasma expansion (at 400 ns), in the initial stage of plasma formation (at 20 ns), the continuum radiation caused by bremsstrahlung and radiative recombination [29] was stronger, which resulted in the lower signal-to-background ratios of emission lines. In order to improve the reliability of experimental results of species distribution, not only each image was accumulated 60 times, but also different ICCD gains were used for species imaging. It can be seen from Fig. 3 that the plasma induced by low irradiance laser (1 GW/cm^2) exhibits an obvious layer structure during its initial expansion, and there is a clear borderline between the species of Ar from the ambient gas and the other species from the target. This is because the laser irradiance was too small to reach the excitation threshold of argon, and the argon was almost transparent to the laser. The laser could be directly deposited on the vapor plasma and absorbed by it. The excitation and ionization of argon was due to the interaction of compression, thermal conduction and radiative transfer between argon and the hot plasma core. The layered distribution of species indicates that the plasma propagation model was LSC-wave dominated at such a low irradiance level.

At high laser irradiance (10 GW/cm^2), as can be seen from Fig. 3, the Ar II species are so widely distributed that they almost overlap with the regions of species coming from the target. In this case, the high ionization degree of shocked background argon was achieved not only

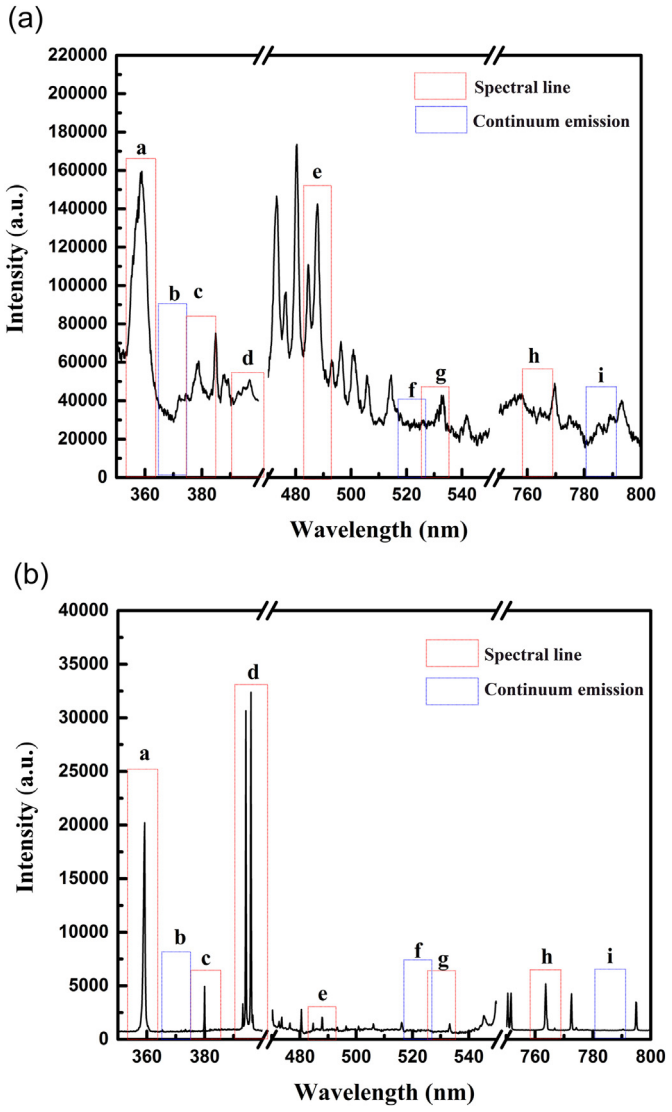

Fig. 2. The spectra of plasma induced from Al–Sn alloy at (a) 20 ns and (b) 400 ns by laser irradiance of 10 GW/cm^2. The letters from "a" to "i" indicate the different spectral lines used for spectroscopic imaging of Al II (a), Al I (d), Sn II (g), Sn I (c), Ar II (e) and Ar I (h) together with spectral bands for imaging with the continuum emission (b, f, i).

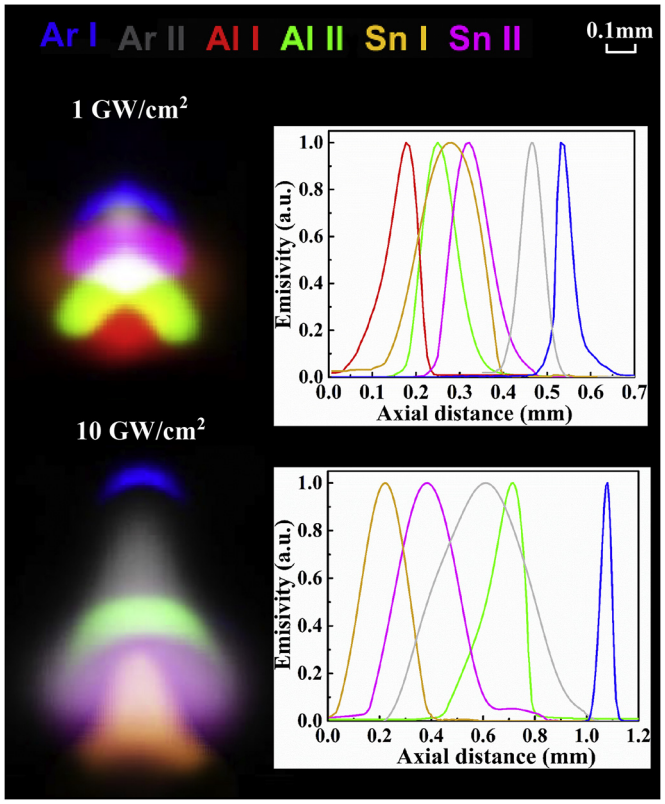

Fig. 3. Emissivity images and normalized central axial emissivity profiles of Ar I, Ar II, Al I, Al II, Sn I, and Sn II species in plasmas produced from the alloy with mass ratio of Al:Sn = 3:7 at 20 ns by laser irradiances of 1 GW/cm^2 and 10 GW/cm^2.

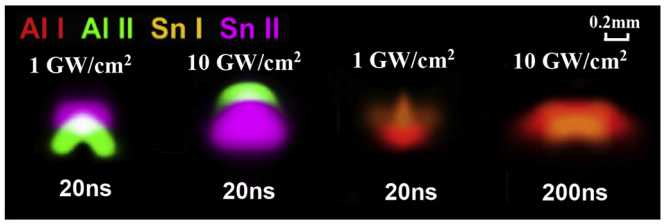

Fig. 4. Emissivity images of Al I, Al II, Sn I, and Sn II species in plasmas induced by laser irradiances of 1 GW/cm^2 and 10 GW/cm^2 at 20 ns or 200 ns.

by interacting with the hot plasma core, but also by directly absorbing a large amount of laser energy. The shocked gas layer propagated forward and backward, forming a mixed region with vapor plasma [11,12]. The overlapped distribution of species indicates that the plasma propagation model was LSD-wave dominated at such a high irradiance level. In addition, because the plasma absorbed energy from the tail of the laser pulse, the shock wave propagated preferentially toward the laser incidence direction, so the plasma appeared to be more slender. Due to the higher ionization degree of plasma, Al atoms were completely ionized at the initial stage of plasma expansion, and the Al I line was emitted after cooling for a period of time.

3.1.2. Dependence on LSA-wave regime

A comparison between the species distributions of Al and Sn in plasmas at 20 ns and 200 ns by the two ablation irradiances is shown in Fig. 4. It should be clarified that in the case of high laser irradiance, the Al atoms did not appear until 200 ns due to the lower ionization energy of Al I (6.01 eV) in comparison with those of Sn I (7.36 eV) and Ar I (15.81 eV). They were completely ionized at the initial stage of plasma expansion, and the Al I line was emitted after cooling for a period of time. It can be seen that there is a significant difference in the species distribution between the two initial plasmas. At low irradiance, the species layers of Al are distributed below those of Sn, while at a high irradiance, they are the opposite. The similar phenomenon was mentioned for miscible Cu–Zn alloy by Bulatov et al. [20] and Borisov et al. [30], who suggested that Zn is present at an outer shell, while Cu is present mainly in an inner shell. This feature is in agreement with the physical intuition, since both the melting and boiling points of Zn are lower. However, in the case of immiscible Al–Sn alloys, the melting point of Sn is lower but the boiling point is higher than that of Al. Whether such a species distribution in the plasma of immiscible alloy depends on the melting point or boiling point is discussed in detail below.

When the low irradiance laser was irradiated on the alloy, a sharp temperature jump occurred initially in a volume near the surface defined by the laser irradiance. This heat was transported away from the surface on a time scale characterized by the thermal diffusivity of the solid, which for metals is short in comparison to a several ns laser pulse duration. A time-varying temperature gradient was then established in the material. When the surface reached the melting point of the solid, a

melt front started to move into the solid. Thus for the LSC-wave dominated plasma, the incident laser usually causes a melting process on the sample surface. Examination of solid-liquid binary-phase diagrams for Al—Sn alloy showed that some systems of elements were immiscible above certain temperatures [31]. In other words, an element will segregate from a solid mixture into a pure liquid when the temperature rises above the melting point of the element [31]. For example, Cu in Zn, Pb in A1, Sn in A1 and so on. This phenomenon is called "zone refinement", in which the virtually instantaneous migration and segregation of elements during melting of the sample provides an enriched element from which molten droplets are ejected [32]. Zone refinement will appear when Al—Sn alloy ablated by low irradiance laser. The Sn species with a lower melting point were firstly melted away from the sample, causing them to be distributed at the top of the plasma. Cromwell et al. [31] also proved the existence of zone refinement of Sn during the ablation of aluminum SRM 1256A with low-fluence ablation. Their further examination on the binary-phase diagrams of A1-Sn systems showed that there was complete segregation of liquid Sn from A1 above 230 °C.

When the laser irradiance was sufficiently high, the alloy surface temperature exceeded the boiling point and a second phase front started to propagate [31]. Thus for the LSD-wave dominated plasma, the excessive laser irradiation directly vaporized all the species on the alloy surface. Since Al and Sn species have similar boiling points, they were vaporized almost simultaneously. In this way, the species distribution in plasma mainly depends on the velocity of each species. The relative atomic mass of Al is smaller than that of Sn, thus the Al species moved faster and were distributed in the upper part of the plasma.

In summary, we have derived two conclusions: 1) the species distribution of LSC-wave dominated plasma mainly depends on the melting points of the constituted elements in immiscible alloys, 2) the species distribution of LSD-wave dominated plasma mainly depends on the atomic masses of the constituted elements.

3.1.3. Validation

In order to further validate the above two conclusions, more theoretical and experimental studies have been carried out on species distribution under different LSA-wave regimes.

The spectral diagnosis was employed to verify the conclusion. The amplified images of the plasmas produced from the alloy with mass ratio of Al:Sn = 3:7 at 400 ns by laser irradiances of 1 GW/cm^2 and 10 GW/cm^2 were scanned point by point by the fiber along x axis of plume expansion at $r = 0$ with 0.5 mm step size. The reason for choosing such a long delay is that the order of species layers in plasma dose not change with time [25], and the initial plasma usually devites from the local thermodynamic equilibrium [33]. Theoretically, the intensity ratio of Sn II (533.23 nm) and Al II (358.66 nm) can be expressed as

$$\frac{I_{Sn}}{I_{Al}} = \frac{N_{Sn} U_{Al}(T) \lambda_{nm,Al} A_{ki,Sn} g_{k,Sn}}{N_{Al} U_{Sn}(T) \lambda_{ki,Sn} A_{nm,Al} g_{n,Al}} \exp\left(\frac{E_{n,Al} - E_{k,Sn}}{k_b T}\right), \quad (1)$$

where I_{Sn} is the line intensity from the k-i transition and I_{Al} is that from the n-m transition, N is the number density, $U(T)$ is the partition function for the emitting species, λ is the wavelength, A is the transition probability, g is the degeneracy, E_n and E_k are the upper level energies, k_b is the Boltzmann constant, and T is the plasma temperature. Then the corresponding number density ratio can be calculated by

$$\frac{N_{Sn}}{N_{Al}} = \frac{I_{Sn} U_{Sn}(T) \lambda_{ki,Sn} A_{nm,Al} g_{n,Al}}{I_{Al} U_{Al}(T) \lambda_{nm,Al} A_{ki,Sn} g_{k,Sn}} \exp\left(\frac{E_{k,Sn} - E_{n,Al}}{k_b T}\right). \quad (2)$$

Fig. 5 depicts the normalized number density ratio of ionic species of Sn and Al along x axis. Here, the plasma temperatures were calculated from the Boltzmann plots of atomic Al lines at 308.22 nm, 309.27 nm, 394.40 nm and 396.15 nm. A representative example of Boltzmann plot at $x = 0.6$ mm and $r = 0$ mm of the plasma produced from the alloy with mass ratio of Al:Sn = 3:7 by laser irriadiance of 1 GW/cm^2 is shown in Fig. 6, where the slope gives $T = 5476 \pm 600$ K. The electron temperature along x axis was estimated to be in the range of 5012–5880 K for 1 GW/cm^2 and 5520–6768 K for 10 GW/cm^2. It can be seen from Fig. 5 that the maximum ratio appears at $x = 0.6$ mm for 1 GW/cm^2 and at $x = 0.3$ mm for 10 GW/cm^2. This indicates that the Sn ions are mainly distributed in the top of LSC-wave dominated plasma, while in LSD-wave dominated plasma, they are distributed near the bottom. Thus for LSC-wave dominated plasma, species with lower melting point are preferentially separated from the sample during laser ablation and enriched at the top of the plasma. In other words, laser ablation of immiscible alloy formed by elements with very different melting points may cause fractionation, and the element with lower melting point will be distributed at an upper shell.

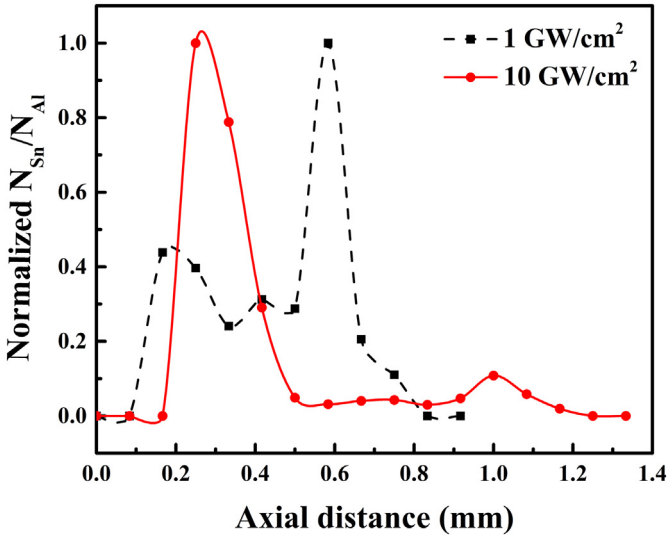

Fig. 5. Normalized number density ratio of ionic Sn and Al species along x axis of the plasma produced from the alloy with mass ratio of Al:Sn = 3:7 at 400 ns by laser irradiances of 1 GW/cm^2 and 10 GW/cm^2.

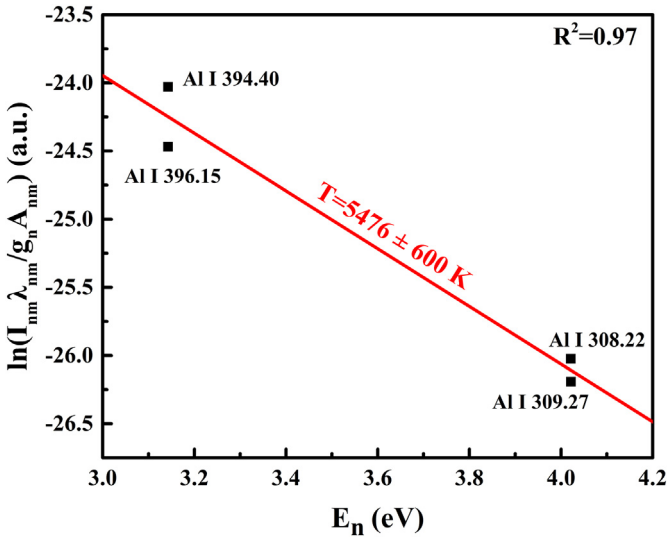

Fig. 6. Boltzmann plot of Al I lines at $x = 0.6$ mm and $r = 0$ mm of the plasma produced from the alloy with mass ratio of Al:Sn = 3:7 by laser irriadiance of 1 GW/cm^2 at 400 ns.

The plasma dynamics theory was employed to verify the second conclusion. The total velocity of a species in a LSD-wave dominated plasma can be described as [34].

$$v_{tot} = v_t + v_e + v_c, \quad (3)$$

where $v_t = \sqrt{3kT/m}$ is the thermal velocity, $v_e = \sqrt{1.67kT/m}$ is the plasma expansion velocity according to the adiabatic expansion model in vacuum, $v_c = \sqrt{2ev_0/m}$ is the Coulomb velocity for singly ionized ions, k is the Boltzmann constant, T is the temperature, m is the species mass, and v_0 is the equivalent acceleration voltage. According to the formula, the movement velocity of a species is inversely proportional to the square root of its mass. As a result, the movement velocity of Al species in the plasma was about twice as fast as Sn species, and they were distributed in the upper layer of the plasma. This is consistent with the view of Min et al. [35], who theoretically and experimentally demonstrated that the velocity of C II species was higher than that of Si II in the plasma induced from the SiC target in a vacuum chamber.

3.2. Dependence on sample composition

LIBS is a spectrochemical quantitative analysis technique by taking advantages of spectral lines emitted from species in the plasma. Studying the influence of sample composition on species distribution in plasma may provide guidance for further improving its quantitative performance.

The emissivity images and normalized central axial emissivity profiles of Al I, Al II, Sn I, and Sn II species in plasmas produced from the three alloys by laser irradiances of 1 GW/cm^2 and 10 GW/cm^2 at 400 ns are shown in Fig. 7. The reason for choosing such a large delay is that under the high laser irradiance, the ionization degree of plasma was so high that for the plasma induced from the alloy with mass ratio of Al: Sn = 7:3, the Al atoms did not appear until 400 ns. It can be seen from Fig. 7(a) that for LSC-wave dominated plasmas, although the sample compositions are different, the distribution orders of species are the same. From top to bottom of the plasma, the order is always Sn II, Al II, Sn I, and Al I species. Similarly, for LSD-wave dominated plasmas shown in Fig. 7(b), the order is always Al II, Sn II, Al I, and Sn I species. Therefore, under the same LSA-wave regime, the plasmas produced from binary alloys with different mass ratios of constituted elements have the same order of species distribution. This illustrates that, unlike laser irradiance, the mass ratio of elements in binary samples does not change the species distribution of plasma.

4. Conclusions

Spectrally, spatially and temporally resolved imaging was used to obtain the emissivity images of the plasmas induced by near-infrared laser from binary alloys to observe the process of plasma expansion into ambient gas. These emissivity images reflect the relative distribution of various species in the plasma and the temporal evolution process intuitively. The dependence of species distribution in plasma produced from binary alloy on LSA-wave regime and sample composition has been studied. It is found that laser irradiance can change the spatial distribution of species in plasma, while the sample composition cannot. At relatively low laser irradiance, in which case the plasma propagation is characterized by LSC-wave, the melting point is the key factor that determines the relative species distribution in initial plasma. For

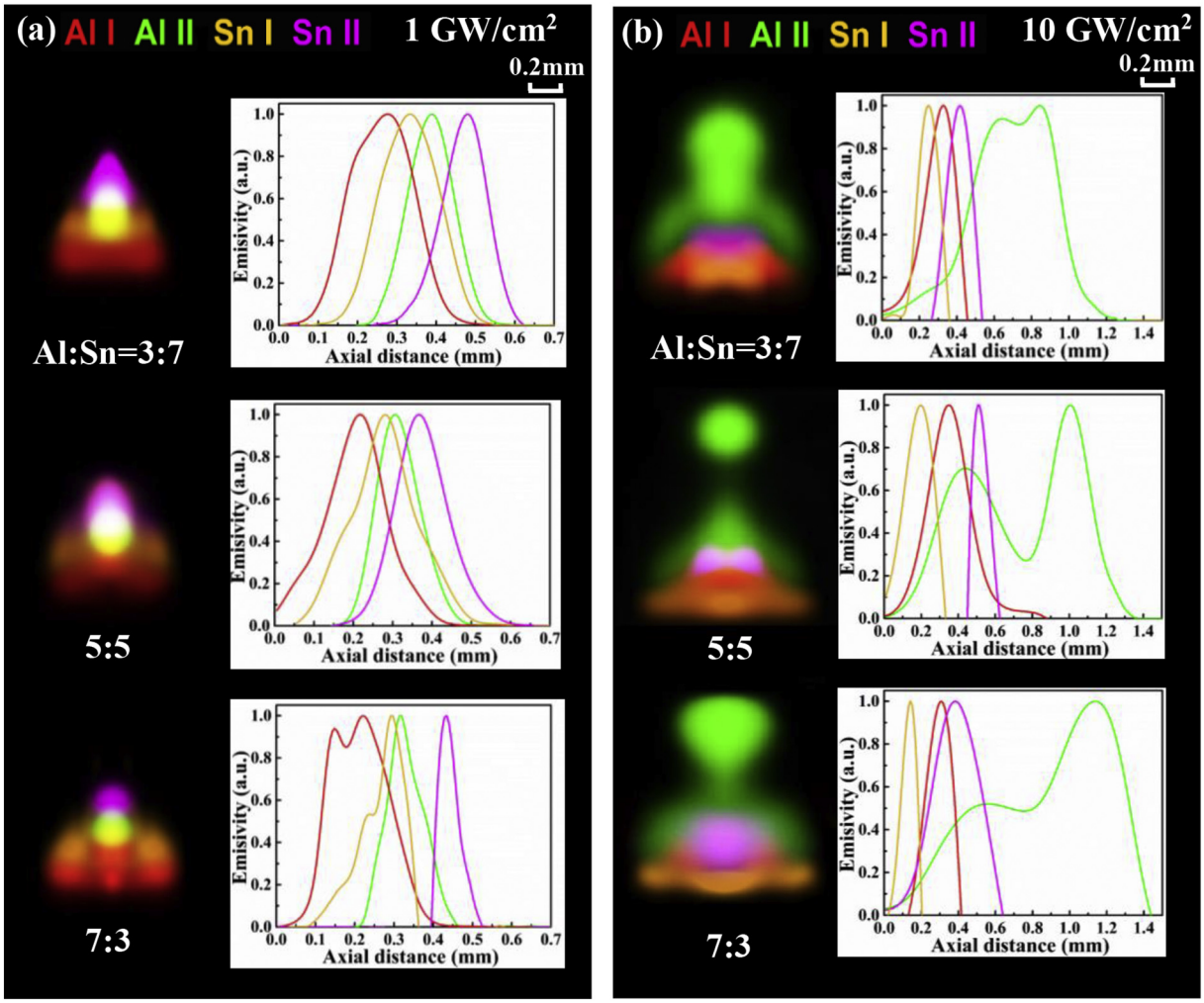

Fig. 7. Emissivity images and normalized central axial emissivity profiles of Al I, Al II, Sn I, and Sn II species in plasmas produced from alloys with mass ratios of Al to Sn of 7:3, 5:5, and 3:7 at 400 ns by laser irradiances of (a) 1 GW/cm^2 and (b) 10 GW/cm^2.

immiscible alloys, species with lower melting point are preferentially separated from the sample during laser ablation and distributed at an upper shell of the plasma. At high laser irradiance, when the plasma propagation exhibits characteristics corresponding to LSD-wave, the atomic mass becomes a key factor that determines the relative species distribution in plasma. Species with smaller atomic mass have the faster movement velocity and are distributed at an upper shell of the plasma. In each LSA-wave propagation regime, the sample composition does not change the species distribution of plasma. Overall, this work reveals the dependence of species distribution on LSA-wave regime and sample composition in laser-induced plasmas produced from binary alloy, and we think that it might be generally suitable for other elements or even multi-element plasmas.

Acknowledgement

This work was supported by the National Key R&D Program of China (2017YFA0304203); the Changjiang Scholars and Innovative Research Team in University of Ministry of Education of China (IRT_17R70); the National Natural Science Foundation of China (NSFC) (61875108, 61775125, 11434007); the Major Special Science and Technology Projects in Shanxi (MD2016-01, 201804D131036); the 111 project (D18001); and the Fund for Shanxi “1331KSC”.

References

[1] J.D. Winefordner, I.B. Gornushkin, T. Correll, E. Gibb, B.W. Smith, Comparing several atomic spectrometric methods to the super stars: special emphasis on laser induced breakdown spectrometry, LIBS, a future super star, J. Anal. Atom. Spectrom. 19 (9) (2004) 1061–1083.
[2] Z.Y. Hou, Z. Wang, T.B. Yuan, J.M. Liu, Z. Li, W.D. Ni, A hybrid quantification model and its application for coal analysis using laser induced breakdown spectroscopy, J. Anal. At. Spectrom. 31 (3) (2016) 722.
[3] R. Noll, V. Sturm, Ü. Aydin, D. Eilers, C. Gehlen, M. Höhne, A. Lamott, J. Makowe, J. Vrenegor, Laser-induced breakdown spectroscopy-from research to industry, new frontiers for process control, Spectrochim. Acta Part B 63 (10) (2008) 1159–1166.
[4] M. Gaft, E. Dvir, H. Modiano, U. Schone, Laser induced breakdown spectroscopy machine for online ash analysis in coal, Spectrochim. Acta Part B 63 (10) (2008) 1177–1182.
[5] F.Z. Dong, X.L. Chen, Q. Wang, L.X. Sun, H.B. Yu, Y.X. Liang, J.G. Wang, Z.B. Ni, Z.H. Du, Y.W. Ma, J.D. Lu, Recent progress on the application of LIBS for metallurgical online analysis in China, Front. Phys. 7 (6) (2012) 679–689.
[6] Y.P. Raĭzer, Breakdown and heating of gases under the influence of a laser beam, Soviet Phys. Usp. 8 (5) (1966) 650–673.
[7] J.W. Daiber, H.M. Thompson, Laser-driven detonation waves in gases, Phys. Fluids 10 (6) (1967) 1162.
[8] M.H. Key, Ionization effects in a hydrodynamic model of radiation-driven breakdown wave propagation, J. Phys. B 2 (5) (1969) 544–550.
[9] J.E. Lowder, D.E. Lencioni, T.W. Hiiron, R.J. Hull, High-energy pulsed CO2-laser-target interactions in air, J. Appl. Phys. 44 (6) (1973) 2759–2762.
[10] D.A. Cremers, L.J. Radziemski, Handbook of Laser-Induced Breakdown Spectroscopy, John Wiley & Sons, 2013.
[11] J. Yu, Q.L. Ma, V. Motto-Ros, W.Q. Lei, X.C. Wang, X.S. Bai, Generation and expansion of laser-induced plasma as a spectroscopic emission source, Front. Phys. 7 (6) (2012) 649–669.
[12] R.G. Root, Laser-Induced Plasmas and Applications, Dekker, New York, 1989 (Chap. 2).
[13] G. Cristoforetti, G. Lorenzetti, S. Legnaioli, V. Palleschi, Investigation on the role of air in the dynamical evolution and thermodynamic state of a laser-induced aluminium plasma by spatial- and time-resolved spectroscopy, Spectrochim. Acta B 65 (9) (2010) 787–796.
[14] J.A. Aguilera, C. Aragón, J. Bengoechea, Spatial characterization of laser-induced plasmas by deconvolution of spatially resolved spectra, Appl. Opt. 42 (30) (2003) 5938–5946.
[15] E.M. Monge, C. Aragón, J.A. Aguilera, Space- and time-resolved measurements of temperatures and electron densities of plasmas formed during laser ablation of metallic samples, Appl. Phys. A Mater. Sci. Process. 69 (1) (1999) S691–S694.
[16] J.A. Aguilera, C. Aragón, Characterization of a laser-induced plasma by spatially resolved spectroscopy of neutral atom and ion emissions. Comparison of local and spatially integrated measurements, Spectrochim. Acta B 59 (12) (2004) 1861–1876.
[17] J.A. Aguilera, C. Aragón, Characterization of laser-induced plasma during its expansion in air by optical emission spectroscopy: observation of strong explosion self-similar behavior, Spectrochim. Acta B 97 (9) (2014) 86–93.
[18] C. Aragón, F. Peñalba, J.A. Aguilera, Spatial distributions of the number densities of neutral atoms and ions for the different elements in a laser induced plasma generated with a Ni-Fe-Al alloy, Anal. Bioanal. Chem. 385 (2) (2006) 295–302.
[19] C. Aragón, F. Peñalba, J.A. Aguilera, Spatial characterization of laser-induced plasmas: distributions of neutral atom and ion densities, Appl. Phys. A Mater. Sci. Process. 79 (4–6) (2004) 1145–1148.
[20] V. Bulatov, L. Xu, I. Schechter, Spectroscopic imaging of laser-induced plasma, Anal. Chem. 68 (17) (1996) 2966–2973.
[21] R.A. Al-Wazzan, J.M. Hendron, T. Morrow, Spatially and temporally resolved emission intensities and number densities in low temperature laser-induced plasmas in vacuum and in ambient gases, Appl. Surf. Sci. 96 (95) (1996) 170–174.
[22] D.A. Cremers, L.E. Foster, M.J. Ferris, R.A. Multari, Effect of sampling geometry on elemental emissions in laser-induced breakdown spectroscopy, Appl. Spectrosc. 50 (12) (1996) 1483–1499.
[23] V. Motto-Ros, Q.L. Ma, S. Grégoire, W.Q. Lei, X.C. Wang, F. Pelascini, F. Surma, V. Detalle, J. Yu, Dual-wavelength differential spectroscopic imaging for diagnostics of laser-induced plasma, Spectrochim. Acta B 74–75 (2012) 11–17.
[24] Q.L. Ma, V. Motto-Ros, X.S. Bai, J. Yu, Experimental investigation of the structure and the dynamics of nanosecond laser-induced plasma in 1-atm argon ambient gas, Appl. Phys. Lett. 103 (20) (2013) 204101.
[25] X.S. Bai, Q.L. Ma, M. Perrier, V. Motto-Ros, D. Sabourdy, L. Nguyen, A. Jalocha, J. Yu, Experimental study of laser-induced plasma: influence of laser fluence and pulse duration, Spectrochim. Acta B 87 (9) (2013) 27–35.
[26] X.S. Bai, F. Cao, V. Motto-Ros, Q.L. Ma, Y.P. Chen, J. Yu, Morphology and characteristics of laser-induced aluminum plasma in argon and in air: a comparative study, Spectrochim. Acta B 113 (2015) 158–166.
[27] M. Boueri, M. Baudelet, J. Yu, X.L. Mao, S.S. Mao, R. Russo, Early stage expansion and time-resolved spectral emission of laser-induced plasma from polymer, Appl. Surf. Sci. 255 (2009) 9566–9571.
[28] S.L. Ma, H.M. Gao, L. Wu, Modified fourier-hankel method based on analysis of errors in abel inversion using fourier transform techniques, Appl. Opt. 47 (9) (2008) 1350–1357.
[29] A.D. Giacomo, R. Gaudiuso, M. Dell’Aglio, A. Santagata, The role of continuum radiation in laser induced plasma spectroscopy, Spectrochim. Acta B 65 (5) (2010) 385–394.
[30] O.V. Borisov, X.L. Mao, A. Fernandez, M. Caetano, R.E. Russo, Inductively coupled plasma mass spectrometric study of non-linear calibration behavior during laser ablation of binary Cu-Zn alloys, Spectrochim. Acta B 54 (9) (1999) 1351–1365.
[31] E.F. Cromwell, P. Arrowsmith, Fractionation effects in laser ablation inductively coupled plasma mass spectrometry, Appl. Spectrosc. 49 (11) (1995) 1652–1660.
[32] P.M. Outridge, W. Doherty, D.C. Gregoire, The formation of trace element-enriched particulates during laser ablation of refractory materials, Spectrochim. Acta B 51 (12) (1996) 1451–1462.
[33] G. Cristoforetti, A.D. Giacomo, M. Dell’Aglio, S. Legnaioli, E. Tognoni, V. Palleschi, N. Omenetto, Local thermodynamic equilibrium in laser-induced breakdown spectroscopy: beyond the McWhirter criterion, Spectrochim. Acta B 65 (1) (2010) 86–95.
[34] L. Torrisi, D. Margarone, Investigations on pulsed laser ablation of Sn at 1064 nm wavelength, Plasma Sources Sci. Technol. 15 (2006) 635–641.
[35] Q. Min, M.G. Su, S.Q. Cao, D.X. Sun, G. O’Sullivan, C.Z. Dong, Dynamics characteristics of highly-charged ions in laser-produced SiC plasmas, Opt. Express 26 (6) (2018) 7176–7189.